High thermoelectric performance of layered LaAg*X*O (*X* = Se, Te) from electrical and thermal transport calculations

Arul Raj Natarajan,[1] L. Ponvijayakanthan,[1] Mayanak K. Gupta [ORCID],[2,3] Ranjan Mittal [ORCID],[2,3] David J. Singh [ORCID],[4] and V. Kanchana [ORCID][1,*]

[1]*Department of Physics, Indian Institute of Technology Hyderabad, Kandi-502285, Sangareddy, Telangana, India*
[2]*Solid State Physics Division, Bhabha Atomic Research Centre Trombay, Mumbai 400085, India*
[3]*Homi Bhabha National Institute, Anushaktinagar, Mumbai 400094, India*
[4]*Department of Physics and Astronomy, University of Missouri, Columbia, Missouri 65211-7010, USA*

The present paper reports the electronic structure, thermal and electronic transport properties of layered oxychalcogenides LaAg*X*O (*X* = Se, Te) using density functional theory. Different scattering mechanisms, such as acoustic deformation scattering (ADP), ionized impurity scattering (IMP), and polar optical scattering (POP) are included to calculate the scattering rates at various doping concentrations and temperatures. The calculated scattering rates are used in the Boltzmann transport equation to get the absolute values of thermoelectric coefficients. The Seebeck coefficient of both the compounds is nearly 400 μV/K for optimal *p*-type doping. The lattice thermal conductivity of both LaAg*X*O is ultralow with values around 0.20 W/mK along the "*c*" axis at 300 K due to low lifetime and low group velocity. This is lower than other well-known thermoelectric materials, such as PbTe and SnSe. Rattling motion observed in the Ag-Te tetrahedral layer might be the reason for the significant suppression of κ_l. We predict huge *ZT* values of 1.63 for *p*-type and 2.8 for *n*-type LaAgTeO at 900 K, which are higher than that of promising thermoelectric materials, such as BiCuSeO (1.4) and LaCuSeO (2.71). There is a crossing in phonon band dispersion which forms a nodal line on the 001 plane that may lead to topological behavior. This study highlights LaAg*X*O as potential thermoelectric materials for future device applications.

I. INTRODUCTION

The thermoelectric effect describes a material's ability to create electric power when subjected to a thermal gradient without moving components [1–3]. Thermoelectric generators offer a promising way to boost the efficiency of numerous processes with applications in power production, household products, transportation, wearable gadgets driven by human body heat and solid-state refrigeration [4–7]. A thermoelectric material's efficiency is characterized by the dimensionless thermoelectric figure of merit (*ZT*), given by $ZT = \frac{S^2\sigma}{(k_l+k_e)}T$ where "*S*" is thermopower, "σ" is electrical conductivity, "*T*" is temperature, and "κ_l" and "κ_e" are the lattice and electronic contributions to the thermal conductivity, respectively [8]. A good thermoelectric material should possess a large thermopower as well as high electrical conductivity and low thermal conductivity. The power factor PF $= \sigma S^2$ is an important parameter for any thermoelectric material. Materials with high power factor along with high *ZT* has been sought after for thermoelectric device applications. Unfortunately, improving the power factor and *ZT* is particularly challenging due to the conflicting needs of material properties to increase *S* and σ simultaneously. However, due to continuous effort from scientists across the world, a high figure of merit greater than one has been achieved in state-of-the-art materials, such as Bi_2Te_3, PbTe, and SnSe operating at temperatures ranging from room temperature to midhigh temperature. But the disadvantage of these materials are that they are easily oxidized, deteriorated, or decomposed at high temperatures and some of them include hazardous elements.

Oxychalcogenides have recently piqued the interest of the thermoelectric community due to their structural, chemical, and thermal stability even at high temperatures [9]. As a result, these materials have been identified as being more suitable for thermoelectric and other functional applications [10,11]. Many oxychalcogenides crystallize on tetragonal ZrCuSiAs-like structures, which belong to the layered material family. A number of thermoelectric studies have been conducted using these so-called 1111 phase materials [12–14]. Generally, the layered structures are favorable for TE applications due to their often large phonon anharmonicity which leads to low lattice thermal conductivity. Layered structures can also lead to a high Seebeck coefficient because of reduced dimensionality. However, the out-of-plane conductivity of van der Waal's layered materials are usually very low due to lack of effective bonding between adjacent layers. Therefore, layered materials with relatively strong interlayer coupling are desirable since they may have high electrical conductivity but low thermal conductivity which would lead to large *ZT* values [13,15]. Therefore, layered oxychalogenide materials could be a good candidate for achieving high thermopower and low ther-

*kanchana@phy.iith.ac.in

mal conductivity [15–17]. In recent years, lanthanum-based 1111-like structure materials have attracted interest due to the relatively high *ZT* in some compounds [18,19]. Lanthanum-based 1111-like structures can have good intrinsic electrical conductivity which can be further controlled by doping with suitable elements. For example, the predicted *ZT* value of some compounds of the same family, such as LaCuOSe (2.71) [13], LaZnOP (2.10) [14], and LaZnOAs (1.92) [14] are promising.

Generally, for transport studies, the Boltzmann transport theory is employed often with the constant relaxation time approximation, which does not separately consider different scattering mechanisms [20]. Consideration of different scattering mechanisms is important for the temperature dependence. So it is necessary to account for various scattering processes in the calculations to predict the thermoelectric properties more accurately. The structural and electronic properties of LaAgSeO have been reported showing the material to be a semiconductor with a complex band structure, but direction-dependent thermoelectric properties are not yet reported [21]. This and the considerations above-mentioned points suggest investigation of its thermoelectric properties. The paper is organized as follows: Section II has the computational methods, Sec. III contains the results and discussion, and Sec. IV concludes the paper.

II. COMPUTATIONAL DETAILS

First-principles calculations were performed by using density functional theory (DFT), as implemented in the Vienna *ab initio* simulation package (VASP) code [22–25]. We used the Perdew-Burke-Ernzerhof generalized gradient approximation (PBE-GGA) [26]. The plane-wave kinetic-energy cutoff is set at 600 eV. In structural optimization, the tolerance values used for energy and force convergence are 10^{-6} eV and 0.01 eV/Å, respectively. A $12 \times 12 \times 6$ Monkhorst-Pack grid is used for self-consistent calculations [27]. Since the GGA underestimates the band gap, we have employed the Heyd-Scuseria-Ernzerhof (HSE) functional for our calculations of electronic properties. Furthermore, for all the electronic structure calculations, the spin-orbit coupling effect has been taken into account as our compounds contain heavy elements. We have also included the van der Waals correction for our calculations with DFT-D3 method as proposed by Grimme *et al.* [28,29] Phonon calculations were performed using the PHONOPY code and density functional perturbation theory (DFPT) as implemented in VASP [30–32]. The phenomenological transport coefficients were calculated using the AMSET code with explicit consideration of *k*-dependent scattering rates based on electron-phonon scattering [33]. Importantly, this allows transport calculations with material-specific detailed scattering at reasonable computational cost. We have performed AMSET calculations for *k*-point meshes of $12 \times 12 \times 6$, $16 \times 16 \times 8$, and $18 \times 18 \times 9$ for *n*-type LaAgTeO, and we have plotted resultant Seebeck coefficients (*S*) and electrical conductivities (*σ*) along the "*a*" and "*c*" directions which is shown in Supplemental Material [34] (Fig. S1). We observed that convergence is reached with $18 \times 18 \times 9$ *k* mesh for these properties. Therefore, we fixed this *k* mesh for our transport calculations. The elastic and mechan-
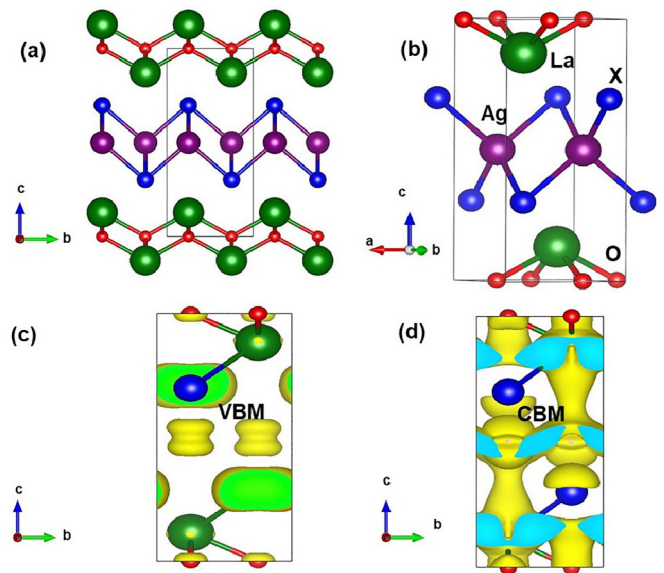

FIG. 1. Crystal structure for LaAg*X*O (*X* = Se, Te) (a) layered form, (b) conventional unit cell and partial charge density for (c) the valence-band minimum (VBM) and (d) the conduction-band maximum (CBM). La, Ag, *X*, and O atoms are shown in green, blue, violet, and red spheres.

ical properties are calculated from the elastic tensor obtained from VASP DFPT calculation using the MechElastic tool [35]. The lattice thermal conductivity calculations were performed using the finite-displacement method implemented in the PHONO3PY package [36]. A supercell of $3 \times 3 \times 2$ is used to calculate the second- and third-order interatomic force constants (IFCs), and we used the default setting for the cutoff pair distance, which meant full elements of third-order anharmonic IFCs were computed. There were 3018 supercells with displaced files each having 144 atoms. To accurately compute the κ_l, the reciprocal spaces were sampled with a $30 \times 30 \times 15$ mesh which is shown in Supplemental Material [34] (Fig. S2).

III. RESULTS AND DISCUSSION

A. Structural, electronic, and mechanical properties

LaAg*X*O (*X* = Se, Te) are oxychalcogenides that are isostructural with promising thermoelectric material BiCuSeO and crystallize in the *P*4/*nmm* space group [37,38]. The crystal structure is shown in Figs. 1(a) and 1(b). It has a tetragonal lattice type with two formula units and eight atoms in the unit cell. The layered structure can be described as alternate stacking of quasi-two-dimensional $[La_2O_2]^+$ and $[Ag_2X_2]^-$ layers along the *c* axis [13]. This framework provides stability along with an anionic conducting layer that can have good electrical properties. Since our compounds are layered, we have employed the Grimme's zero damping DFT-D2 and DFT-D3 methods in structural optimization to account for long-range dispersion forces. The lattice parameters and bonding parameters obtained with and without van der Waals correction are shown in Table I. We found that lattice parameters obtained using the DFT-D3 method are in good agreement with experimental

TABLE I. The calculated equilibrium lattice constants, bond length, and bond angles of LaAg*X*O (*X* = Se, Te).

		a (Å)	c (Å)	V (Å^{-3})	La-O (Å)	La-X (Å)	Ag-X (Å)	X-Ag-X (°)
LaAgSeO	Expt.	4.13	9.30	158.25				
	PBE	4.15	9.42	162.19	2.39	3.36	2.79	116.57
	PBE + DFT-D2	4.11	8.66	146.27	2.36	3.79	2.69	114.51
	PBE + DFT-D3	4.11	9.26	156.20	2.38	3.98	2.76	116.50
LaAgTeO	Expt.	4.23	9.84	176.33				
	PBE	4.25	10.01	180.86	2.42	3.53	2.91	117.88
	PBE + DFT-D2	4.23	9.33	167.13	2.38	3.44	2.82	115.95
	PBE + DFT-D3	4.23	9.64	172.15	2.41	3.45	2.87	117.16

values [21,37]. In La-O layers, the La atoms are coordinated with O atoms in a prismatic manner, whereas, the Ag-*X* layers are made of a network of distorted tetrahedral complexes along the *a-b* plane. From Table I, we can observe that the bond length of La-O is shorter than Ag-*X* which points out that the La ions are closely bonded to O atoms, but the Ag atoms are loosely bonded to *X* atoms.

To explain the different transport characteristics of electrons and holes, we show the band decomposed charge densities around the VBM and CBM in Figs. 1(c) and 1(d) for the examined compounds. The level of the isosurface is set to 0.0001 eÅ^{-3}. Figure 1(c) shows that at the VBM, the states are quite two dimensional. However, charge density is less two dimensional at the CBM [Fig. 1(d)]. As a result, in comparison to electron transport, we can anticipate more anisotropic behaviors in hole transport [9,13]. We have calculated the electron localization function (ELF) to understand the intralayer and interlayer bonding nature of the constituent atoms which is shown in Figs. 2(a) and 2(b). From the ELF figure, we can observe that the intralayer bonding between the Ag-*X* atoms are weaker than the La-O atoms. Moreover, the bonding between the interlayer atoms is also very weak. The tetrahedral complexes of the Ag-Te layer in LaAgTeO were found to be severely distorted from the regular tetrahedron,

resulting in two types of Te-Ag-Te bond angles, 116.50 and 96.16 Å, which are significantly deviated from the uniform tetrahedral bond angle of 109.5 Å [39]. Therefore, in contrast to uniformly bonded homogeneous crystalline solids, Ag-*X* tetrahedra in LaAg*X*O are weakly bonded to the lattice framework which can cause rattling motion [40]. This rattling motion of atoms causes the phonons to scatter more easily which results in reduced lattice thermal conductivity. Therefore, we evaluated the change in potential energy as a function of atomic displacement from their equilibrium positions to investigate whether this prominent anisotropic bonding causes rattling motion, and the results are shown in Figs. 3(a) and 3(b). The potential well along the *x-y* plane directions are shallower than that of along the *z* direction. Furthermore, the potential-energy curves of Ag and *X* atoms are much shallower in the *x* direction which indicates loose bonding of these atoms to lattice framework. These findings point to the possibility of rattling motion as a result of increased anharmonicity [41]. Moreover, the perfect overlap of these shallow potential curves of Ag-Te atoms compared to that of Ag-Se indicates that the tetrahedral Ag-Te could be exhibiting collective rattling motion along the in-plane direction [40]. This behavior indicates that the lattice thermal conductivity along the in-plane direction in LaAgTeO would be less than that of LaAgSeO [42].

We turn to the electronic structure of LaAg*X*O. We have performed the band-structure calculation with both the PBE and the HSE functionals with the inclusion of SOC. The band structures of LaAgSeO and LaAgTeO are shown in Figs. 4(a) and 4(b). Both the compounds have direct band gaps at the high-symmetry point Γ. The band-gap values
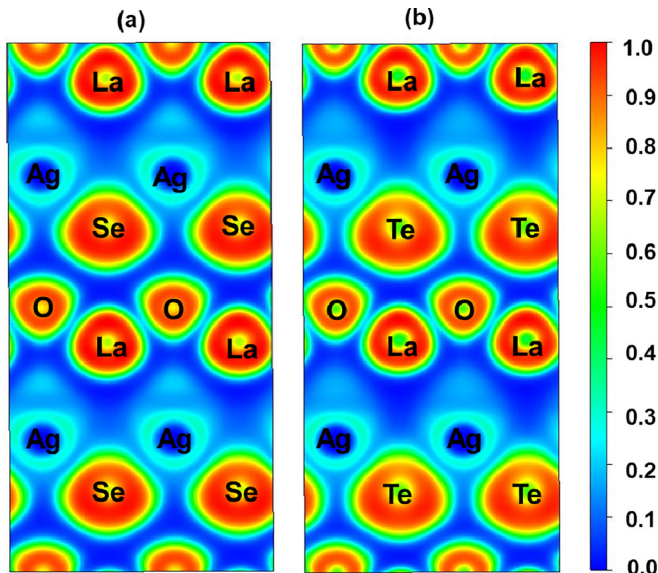

FIG. 2. Electron localization function for (a) LaAgSeO and (b) LaAgTeO along the (100) plane.
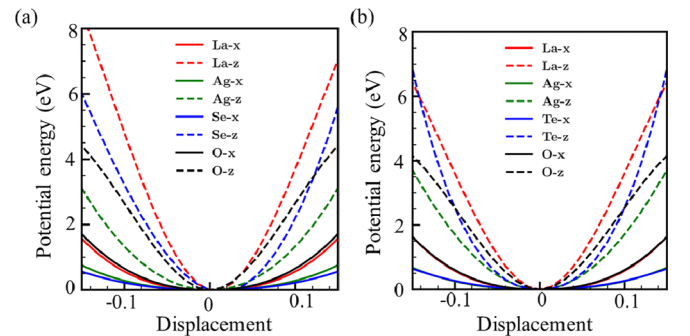

FIG. 3. Calculated potential-energy curves as a function of atom displacement from equilibrium configurations of (a) LaAgSeO and (b) LaAgTeO.
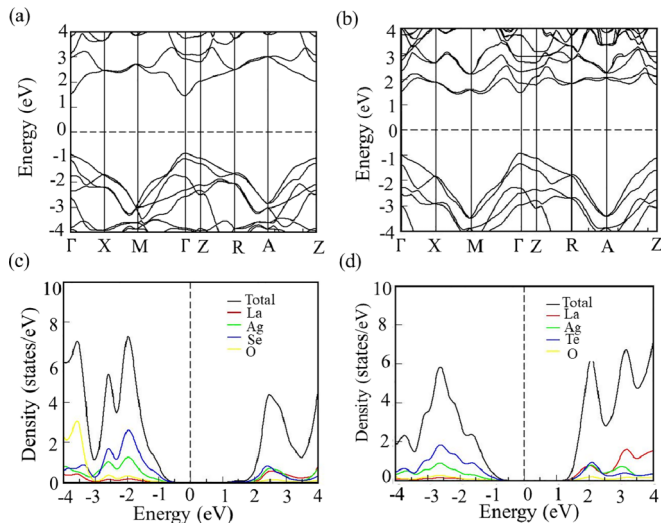
FIG. 4. (a) and (c) Electronic band structure and density of states for LaAgSeO and for (b) and (d) LaAgTeO.

are summarized in Table II. As expected, the band gaps for both compounds have increased significantly with the HSE functional. However, the shapes of the band edges have not changed significantly, which is important for thermoelectricity. The band gap of LaAgSeO has improved from 1.12 eV (PBE) to 2.3 eV (HSE). Similarly, the band gap of the LaAgTeO is improved from 1.29 eV (PBE) to 2.35 eV (HSE). It should be noted that both the PBE and the HSE gaps are large enough that the bipolar effect would be negligible. The electronic density of states (DOS) of LaAgXO are plotted in Figs. 4(c) and 4(d). These density of states show that the chalcogen atoms primarily contribute to the valence band (VB) followed by Ag atoms. Also, we have observed that the VB is primarily composed of X-p and Ag-d orbital characters. For LaAgTeO, the conduction band (CB) is primarily contributed by La atoms with the peak near the CBM being primarily composed of La-f and La-d orbital characters. But, for LaAgSeO, the CBM is dominated by Se-p and Ag-s states. For both compounds, there is a large DOS near the valence-band region.

We have also calculated the effective mass of carriers by parabolic fitting at the VBM and the CBM. We observe that the effective mass of holes are higher than electrons for both the compounds. Correspondingly, the valence bands at the VBM are less dispersive compared to the conduction bands at the CBM. Moreover, the valence band is slightly more dispersive along the in-plane direction Γ-M than the out-of-plane Γ-Z direction. The effective-mass values of holes along

TABLE II. Band-gap (E_g) with the PBE and HSE functionals in eV, effective mass of holes (m_h) and electrons (m_e) in terms of electron rest mass (m_0).

	E_g		m_h		m_e	
	PBE	HSE	a	c	a	c
LaAgSeO	1.12	2.30	0.34	0.90	0.23	0.28
LaAgTeO	1.29	2.35	0.26	1.07	0.23	0.24

the a and c directions also support this point. Therefore, we can expect that the in-plane hole conductivity would be higher than the out-of-plane conductivity. Also the conduction band is strongly dispersive and nearly parabolic at the CBM. The effective-mass values of both directions also nearly same. These imply that there will be less anisotropy in the conductivity of electrons. In LaAgTeO, we see a sharp peak of DOS close to the CBM, whereas in LaAgSeO, we have a modest peak. These high DOS near the band edges could lead to large thermopower [43].

We have also investigated the mechanical properties by calculating the elastic tensor of the compounds. The various elastic moduli, such as the Young modulus (E), the shear modulus (G), and the bulk modulus (B) have been calculated from the elastic constants by the Voigt, Ruess, and Hill approximation theory, and the values are presented in Table III. The tetragonal structure contains six independent elastic constants, according to crystallographic symmetry [44]. The estimated elastic constants for LaAgXO satisfy the Born stability conditions, and the off-diagonal matrix's eigenvalues are positive, indicating that the compounds are mechanically stable. The value of elastic constant C_{11} is greater than C_{33}. This asserts that the a axis is slightly stiffer than the c axis along which the layers are stacked. We have estimated the directional-dependent sound velocities of the longitudinal (v_l) and transverse waves (v_t) using the values of elastic moduli, and these results corroborate with acoustic wave velocities from phonon dispersion, which are given in the Supplemental Material [34] (Table S1). We calculated the Debye temperatures (θ_D) of investigated compounds, which are approximately 265 and 242 K for LaAgSeO and LaAgTeO, respectively [45]. The lower material stiffness reflected in smaller values of B and G leads to lower average velocity of acoustic waves in LaAgTeO. Therefore, it suggests that LaAgTeO would have less lattice thermal conductivity than LaAgSeO based on its elastic characteristics (see Table IV).

B. Phonon and thermal transport properties

The calculated phonon dispersion and density of states of LaAgXO are shown in Fig. 5. The absence of imaginary phonon modes confirms that the studied compounds are dynamically stable. The maximum frequencies observed in LaAgSeO and LaAgTeO are 15.25 and 14.16 THz, respectively, which follows the common trend that the phonon frequency is decreasing with higher atomic mass. The atomic contribution to phonons can be understood from the projected density of states for phonons shown in Figs. 5(c) and 5(d). The contribution to the low-frequency phonon modes arises mainly from La, Ag, and X atoms. Due to the large variation in atomic weights between ions, a gap exists between the low-frequency and high-frequency optical modes. The atomic vibrations of La and O atoms are completely decoupled in the La-O layer where high-frequency optical modes are dominated by O atoms, which are much lighter than La atoms. In the low-frequency range, modes have contribution from La, Ag, and X atoms. We can see from the phonon mode dispersion that the mixing of low-energy optical modes and acoustic modes causes huge peaks in the DOS. This mixing is observed more in the LaAgTeO than LaAgSeO. The low-frequency

TABLE III. The elastic constants C_{ij} and other mechanical properties, such as shear modulus G (GPa), bulk modulus B (GPa), Young's modulus E (GPa) in Hill's approximation, and Poisson's ratio (ν), Density of material ρ (g/mol) and Debye temperature (θ_D) in K.

	C_{11}	C_{11}	C_{13}	C_{33}	C_{44}	C_{66}	B_H	G_H	E	B_H/G_H	ν	ρ	θ_D
LaAgSeO	146.29	63.84	57.29	85.82	33.60	48.04	68.15	33.13	85.54	2.06	0.29	6.99	265.06
LaAgTeO	131.63	66.15	56.56	77.78	33.33	43.24	62.77	30.42	78.58	2.06	0.29	7.16	242.04

onset of optical branches suggests low thermal conductivity, which is due to the anticrossing of phonon branches which lowers the group velocity in these frequency ranges, and increase in the phase space for anharmonic scattering [46]. Furthermore, LaAgTeO exhibits slightly less steeper acoustic branch dispersion around the Γ point compared to LaAgSeO, which is consistent with the elastic characteristics and sound velocities.

The calculated lattice thermal conductivity is shown in Fig. 6(a). Both compounds have low lattice thermal conductivity. LaAgTeO has lower κ_l than LaAgSeO along the *a* direction and along the *c* direction, and both compounds have similar κ_l values. At room temperature, the value of κ_l is 2.02 W/mK for LaAgSeO and the same for LaAgTeO is 1.09 W/mK along the *a* direction. Also the κ_l along the *c* direction for both compounds are nearly 0.2 W/mK. Moreover, we observed ultralow thermal conductivity at elevated temperature for our investigated compounds. At room temperature, the lattice thermal conductivity is comparable to industry standard PbTe [47], SnSe [18], and far lower than most oxide thermoelectrics [48–50].

According to the kinetic theory of lattice thermal conductivity,

$$\kappa_l = \tfrac{1}{3} C_v V_g^2 \tau, \tag{1}$$

where C_v is the lattice specific-heat capacity, V_g and τ are average group velocity and average relaxation time of phonons. Also, from Fig. 6(b), we observed that both compounds' specific-heat capacity do not vary much. We have plotted the group-velocity components of LaAg*X*O as shown in Fig. 7. As we can observe, for both compounds, the group-velocity values of the majority of phonon modes along the in-plane direction are concentrated between the 10^1 and 10^3 m/s range. However, the group velocities of more modes along the out-of-plane *c* direction are less than 10^1 m/s. This implies that the average group velocity along the *c'* direction should be lower than along the *a* direction for both compounds. These results substantiate the low lattice thermal conductivity along the *c* direction. The lifetime of phonon modes of LaAg*X*O

is shown in Figs. 8(a) and 8(b). We observed that the lifetimes of LaAgTeO are lower than LaAgSeO. The phonon lifetimes plot demonstrates acoustic phonons to be mainly responsible for thermal conductivity since the high-frequency optical phonon lifetimes are significantly suppressed [36]. Furthermore, LaAgSeO's larger κ_l value is explained by its somewhat longer phonon lifetimes compared to LaAgTeO. The mean free paths (MFPs) of phonon modes ($\Lambda = v_g \tau$) of both materials are plotted in Fig. 9. In general, the mean free path is lower than several reported low thermal conductivity materials [51]. The low-frequency acoustic modes have a higher mean free path which contributes more to κ_l. We have plotted the Gruneisen parameter for both compounds as shown in Fig. 10. The Gruneisen parameter can be considered as a measure of the anharmonicity of modes. As we can observe from the plots, LaAgTeO has a higher Gruneisen parameter values than LaAgSeO, which reveals that the anharmonicity in LaAgTeO is higher than LaAgSeO [52]. LaAgTeO's lower lattice thermal conductivity can be attributed to this greater anharmonicity. Therefore, our results suggest that the specific-heat capacities (C_v) and group velocities (V_g) of phonons are considerably low for both compounds and have not differed significantly between them. The lifetimes of phonon modes (τ) in these compounds are also generally quite low because of the strong anharmonicity, which increases scattering of phonons. Specifically, the increased anharmonic effects lead to shorter phonon lifetimes in LaAgTeO compared to LaAgSeO, suggesting the reduction in the κ_l of LaAgTeO. This is further proven by the lower mean free path of LaAgTeO compared to LaAgSeO. Overall the

TABLE IV. Materials parameters used to compute scattering rates of LaAg*X*O (*X* = Se, Te). $\epsilon_{s,ij}$ and $\epsilon_{\infty,ij}$ are the static and high-frequency dielectric constants in ϵ_0. D_{ij}^{vb} and D_{ij}^{cb} are the absolute deformation potentials at the valence- and conduction-band edges, respectively. ω_{po} is the effective polar phonon frequency given in terahertz.

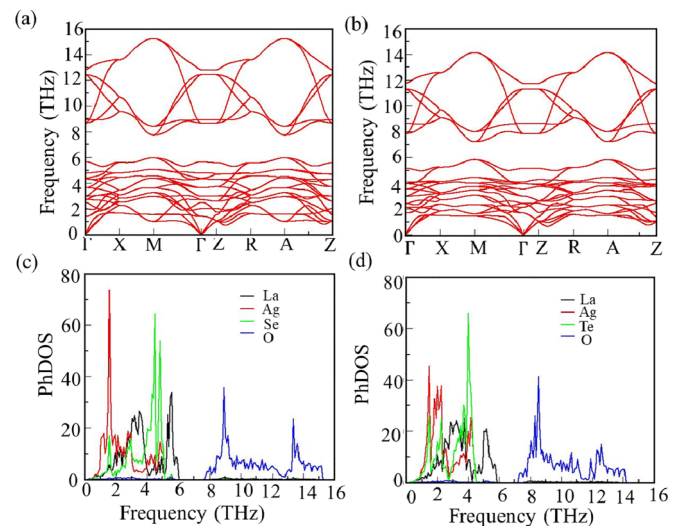|	$\epsilon_{s,11}$	$\epsilon_{s,33}$	$\epsilon_{\infty,11}$	$\epsilon_{\infty,33}$	D_{11}^{vb}	D_{33}^{vb}	D_{11}^{cb}	D_{33}^{cb}	ω_{po}
LaAgSeO	23.70	16.99	7.74	7.34	0.98	2.18	2.71	3.24	5.56
LaAgTeO	21.27	17.94	8.67	8.22	1.83	1.61	3.62	4.47	5.76

FIG. 5. (a) and (c) Phonon dispersion and phonon density of states for LaAgSeO and for (b) and (d) LaAgTeO.
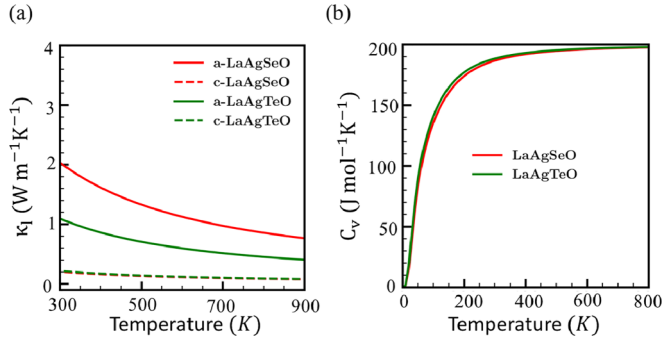
FIG. 6. Calculated (a) lattice thermal conductivity (κ_l) and (b) specific-heat conductivity (c_v) for LaAgXO.

FIG. 8. The calculated lifetime for investigated compounds LaAgXO.

low group velocities and shorter phonon lifetimes characterize the phonon modes in LaAgSeO and LaAgTeO, yielding in short mean free paths thereby lower κ_l values. Such low κ_l is comparable to that of some of the state-of-the-art ultra-low κ_l thermoelectric materials, such as SnSe and BiCuSeO, etc.

To analyze the size dependency and nanostructuring possibility, we have plotted the cumulative lattice thermal conductivity against the MFPs at 300 K as shown in Fig. 11(a). In both LaAgSeO and LaAgTeO, the maximum phonon mean free path is longer in the a direction than in the c direction. Most of the phonon modes that contribute to the lattice thermal conductivity are less than 10 nm. After that critical value, we noted a flattening of the rise of cumulative κ_l, which indicates that modes having MFPs higher than 10 nm are contributing less to the lattice thermal conductivity. These findings also suggest that reducing the lattice thermal conductivity through nanostructuring may not be an effective strategy for our present compounds. Furthermore, Fig. 11(b) shows that modes below 5 THz contribute 50% of the total thermal conductivity. Also, the cumulative thermal conductivity raises about 8–12 THz, indicating that the high-frequency optical
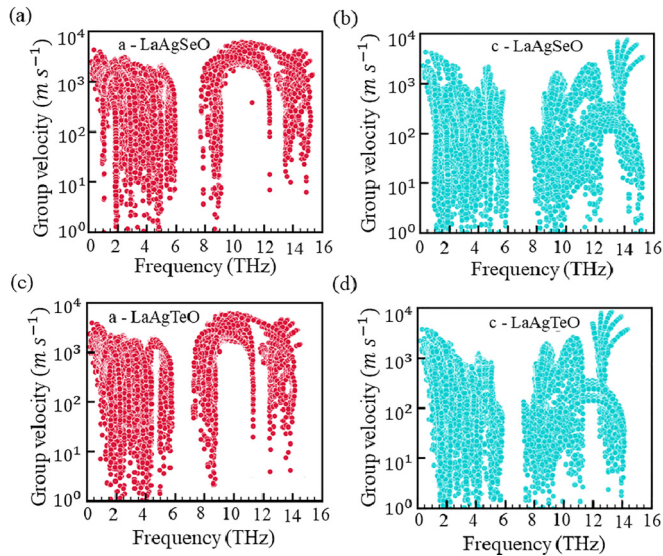
phonons modes coming from the oxygen atoms' vibrations also contribute to the lattice thermal conductivity [53].

Finally, we observed an interesting band crossing in phonon band dispersion along the 001 plane around the frequency value of 4.45 THz for optical phonons of LaAgSeO. In order to verify the optical mode inversion at these crossings, we have performed the symmetry analysis, and found that these modes have mirror eigenvectors A_{2u} and A_{1g}. The opposite mirror eigenvectors ensure the optical mode inversion. To observe the nodal line possibility on this plane, we have plotted the phonon band dispersion along different path between Γ-X and Γ-M for LaAgSeO as shown in Fig. 12. This band crossing is continuous which forms a nodal line on the 001 plane. Similarly, we found for LaAgTeO in 3.24 THz with the mirror eigenvectors of E_u and E_g.

C. Relaxation time of carriers

In this paper, we have used semiclassical transport theory under relaxation time approximation [54,55]. In order to predict the temperature dependence of the transport properties more accurately, we have evaluated the relaxation time by calculating **k**-dependent scattering rates as implemented in the AMSET code [33]. To calculate the scattering rates, we consider the three important scattering processes, such as acoustic deformation scattering (ADP), IMP, and POP. The net scattering rates are added by Matheissen's rule,

$$\frac{1}{\tau_e} = \frac{1}{\tau^{\text{ADP}}} + \frac{1}{\tau^{\text{IMP}}} + \frac{1}{\tau^{\text{POP}}}. \tag{2}$$

FIG. 7. The calculated group-velocity components (a) and (b) for LaAgSeO and (c) and (d) for LaAgTeO along the a and c directions.
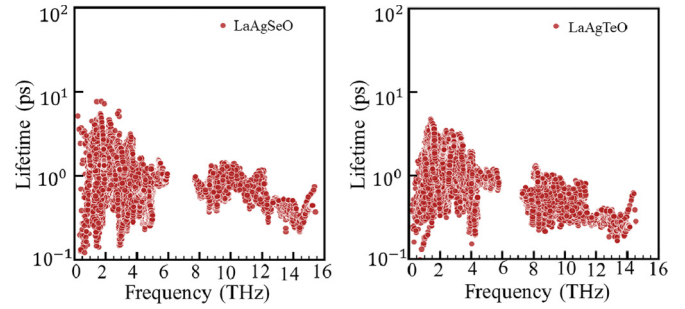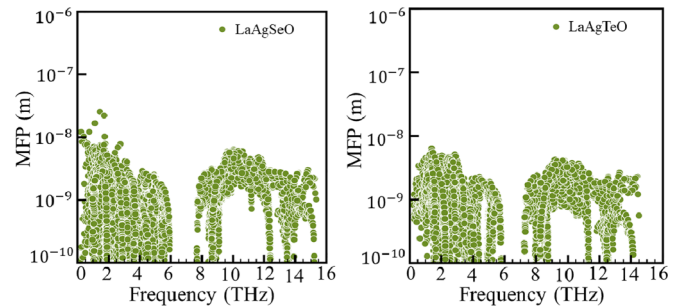

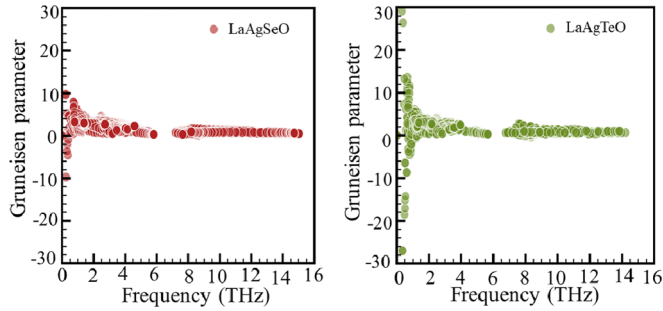FIG. 9. The calculated mean free path for investigated compounds LaAgXO.

FIG. 10. The calculated Gruneisen parameter for investigated compounds LaAgXO.

The scattering rates are calculated using Fermi's golden rule as

$$\tau^{-1}_{n\mathbf{k} \rightarrow m\mathbf{k}+\mathbf{q}} = \frac{2\pi}{\hbar}|g_{nm}|^2\delta(\epsilon_{n\mathbf{k}} - \epsilon_{m\mathbf{k}+\mathbf{q}}), \quad (3)$$

where $n\mathbf{k}$ is an initial wave vector, $m\mathbf{k} + \mathbf{q}$ is the final wave vector after scattering, ϵ is the electron energy, and g is the electron phonon coupling element. Generally, the impact of various mechanisms responsible for scattering of electrons due to phonons expressed by the coupling matrix element,

$$g_{nm}(\mathbf{k}, \mathbf{q}) = \langle m\mathbf{k} + \mathbf{q}|\Delta_q V|n\mathbf{k}\rangle, \quad (4)$$

where $\Delta_q V$ is an electronic perturbation defined by the scattering mechanism.

The long-wavelength acoustic phonons cause the deformation of crystals due to atomic displacements. The deformation potential induced by such static distortion of the lattice scatters the carriers. The matrix elements of this acoustic and optical phonon interaction is calculated using

$$g_{nm}(\mathbf{k}, \mathbf{q}) = \sqrt{k_B T}\left[\frac{\hat{\mathbf{D}}_{n\mathbf{k}:S_l}}{c_l\sqrt{\rho}} + \frac{\hat{\mathbf{D}}_{n\mathbf{k}:S_{t_1}}}{c_{t_1}\sqrt{\rho}} + \frac{\hat{\mathbf{D}}_{n\mathbf{k}:S_{t_2}}}{c_{t_2}\sqrt{\rho}}\right]. \quad (5)$$

Here $D_{nk} = D_{nk} + v_{nk} - S_i D_{nk}$ is a second rank deformation tensor, v_{nk} is the group velocity, S_i is the strain associated with phonon modes, ρ is the density, and c_i are the wave velocities. The subscripts l, t_1, and t_2 indicate properties belonging to the longitudinal and transverse modes. The carriers are also scattered through the microscopic lattice distortion within the unit cell by the long-wavelength optical phonons. The

FIG. 12. (a) Crossing of phonon bands at the inversion points and schematic of nodal line (inside) (b) representation of nodal line in the Brillouin zone.

interaction of the electrons with longitudinal optical phonons is generally modeled as a kind of Frolich interaction with a single effective mode frequency ω_{po}. In this case, the inelastic electron-phonon matrix element is

$$g_{nm}(\mathbf{k}, \mathbf{q}) = \left[\frac{\hbar\omega_{po}}{2}\left(\frac{1}{\hat{\mathbf{q}} \cdot \epsilon_\infty \cdot \hat{\mathbf{q}}} - \frac{1}{\hat{\mathbf{q}} \cdot \epsilon_s \cdot \hat{\mathbf{q}}}\right)\right]^{1/2}xA, \quad (6)$$

where $A = \frac{\langle m\mathbf{k}+\mathbf{q}|n\mathbf{K}\rangle}{|\mathbf{q}|}$ and ϵ_s and ϵ_∞ are the static and high-frequency dielectric tensors. Also the scattering from ionized impurities is treated via the Brooks and Herring model as the screened Coulomb potential with matrix elements given by

$$g_{nm}(\mathbf{k}, \mathbf{q}) = \frac{n_{ii}^{1/2}Ze}{\hat{q} \cdot \epsilon_s \cdot \hat{q}}\frac{\langle m\mathbf{k} + \mathbf{q}|n\mathbf{K}\rangle}{|\mathbf{q}|^2 + \beta^2}, \quad (7)$$

where Z is the impurity charge, e is the electron charge, $n_{ii} = n_h + n_e$ is the concentration of ionized impurities, and β is the inverse screening length.

The calculated scattering rates of hole and electron carriers of LaAgXO are shown in Fig. 13 and also we have tabulated
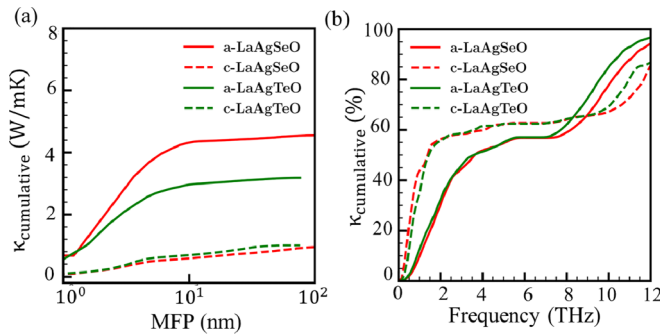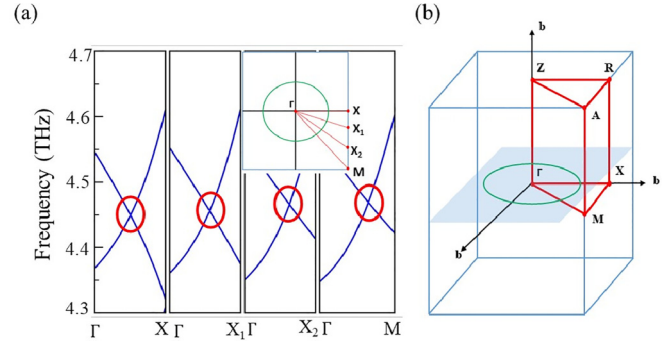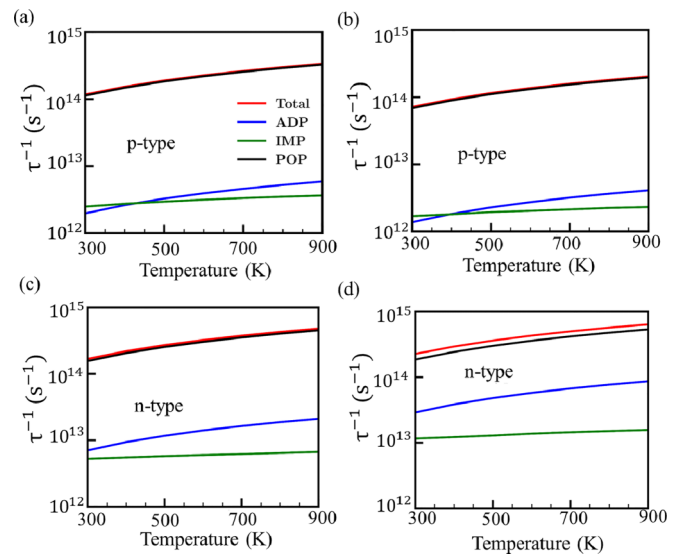

FIG. 11. The calculated cumulative lattice thermal conductivity as a function of (a) phonon mean free path and (b) frequency of investigated compounds LaAgXO.

FIG. 13. Scattering rates as a function of temperature for p-type and n-type carriers at fixed doping concentration 10^{19} cm^{-3} in (a) and (c) for LaAgSeO and (b) and (d) for LaAgTeO.
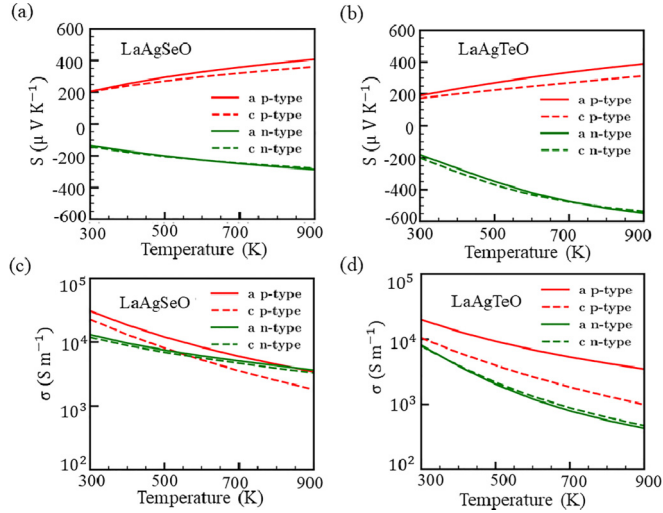
FIG. 14. The thermoelectric coefficients of LaAg*X*O, (a) and (b) Seebeck coefficient (*S*), and (c) and (d) electrical conductivity for LaAgSeO and LaAgTeO, respectively .

FIG. 15. Mobility as a function of temperature for *p*-type and *n*-type carriers at fixed doping concentration 10^{19} cm^{-3} in (a) and (c) for LaAgSeO and (b) and (d) for LaAgTeO.

the material parameters used for the AMSET calculations in Table IV. We observed that POP scattering rates are highly dominating for both holes and electrons [56–58]. For holes, the contributions from IMP and ADP scatterings are almost equal, but for electrons, the contributions from IMP are lower than those from ADP. In general, POP contributes more than 90% of the total scattering rates, whereas both ADP and IMP contribute less than 5% with the exception of *n*-type LaAgTeO for which we observe a larger contribution from both ADP and IMP which is shown in Supplemental Material [34] (Fig. S3). At the optimal doping concentration for both carriers, the overall scattering rates are seen to be in the range of 10^{14}–10^{15} s^{-1}. Furthermore, for both compounds, the scattering rates of *n*-type carriers are larger than those of *p*-type carriers. It should be noted that flat lines are observed for IMP scattering rates since the impurity concentration has been around 10^{19} cm^{-3} for the temperature range. These calculated scattering rates are used to calculate the transport coefficients, which will be discussed in the upcoming section.

D. Thermoelectric properties

The transport properties of LaAg*X*O are investigated based on semiclassical Boltzmann transport theory. The calculated Seebeck coefficient is given in Figs. 14(a) and 14(b). In LaAgSeO, the thermopower of holes is higher than electrons. As a result, LaAgSeO exhibits more promising thermopower for hole doping than electron doping. In LaAgTeO, both carriers exhibit excellent thermopower especially at high temperatures. For instance, the Seebeck coefficient of holes (S_h) is ∼313 μV/K and the Seebeck coefficient of electrons (S_e) is ∼537 μV/K along the *c* direction with the doping concentration of 10^{19} cm^{-3} at 900 K. However, in LaAgTeO as opposed to LaAgSeO, electrons exhibit a greater thermopower than holes. This might be because LaAgTeO has a huge DOS near the CBM than LaAgSeO. Moreover, both compounds generally display similar thermopower for *p*-type doping. The calculated electrical conductivity of both electron and hole
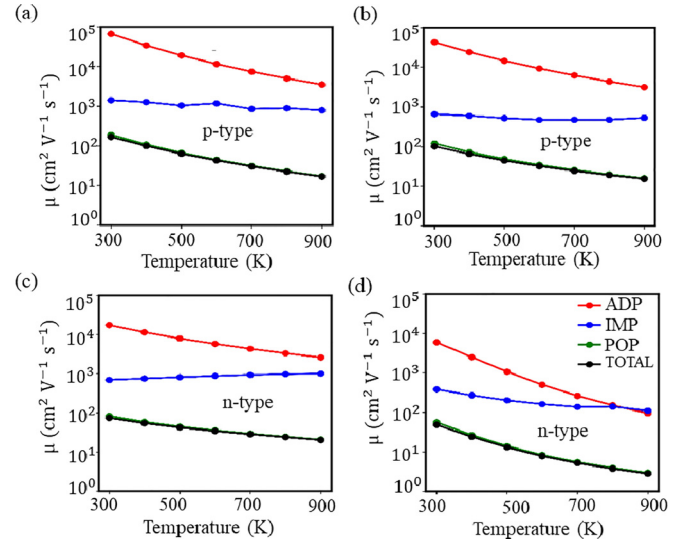
carriers are shown in Figs. 14(c) and 14(d). There is generally a strong anisotropy in hole conductivity between the *a* and the *c* directions with in-plane conductivity being higher than out-of-plane conductivity. However, electron conductivity is virtually isotropic because of the nearly parabolic dispersion of the conduction band at the CBM. Also, the hole conductivity (σ_h) is generally higher than the electron conductivity (σ_e). For instance, in LaAgTeO, at room temperature, σ_h is 17.89×10^3 S/m, whereas, σ_e is 7.25×10^3 S/m with the doping concentration of 10^{19} cm^{-3}. Figure 15 shows the mobility of LaAgSeO and LaAgTeO limited by various scattering processes as well as their total contribution. We observe that the *p*-type mobility is higher than the *n*-type mobility. We would like to point out that mobility is typically based on two variables: the carrier scattering rates as well as the band dispersion and related transport effective mass. Mobility is inversely correlated with both factors. Due to the more dispersive nature of the conduction band, electrons have a lower effective mass than holes (Table II). This should have favored higher mobility of electrons. However, for both compounds, the scattering rates of electrons are higher than holes (Fig. 13). As a result, electrons have less mobility than holes (Fig. 15). This reduced mobility of electron carriers explains the observed lower σ_e compared to σ_h. Also, the electronic thermal conductivity is shown in Fig. 16. We can observe that the κ_e is higher with *p*-type doping than *n*-type doping for both compounds.

Figures 17(a) and 17(b) show the power factor of LaAg*X*O. In both compounds, generally, holes have a higher power factor than electrons, especially along the in-plane direction. In addition, the observed trend of anisotropy between the *a* and *c* directions throughout the Seebeck coefficient and conductivity is also carried over to the power factor. Although the thermopower of holes is seen to be similar for both compounds, the significant increase in conductivity enhanced *p*-type LaAg*X*O's power factor. Overall the power factors of both compounds are promising with *p*-type doping at optimal
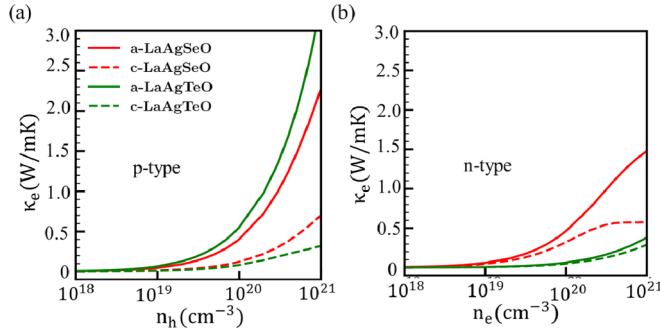
FIG. 16. Calculated electronic thermal conductivity of (a) p-type and (b) n-type LaAgXO.

concentration. Also, the power factors are observed to be large at higher temperatures indicating that these compounds are suitable for high-temperature thermoelectric applications.

E. Figure of merit

In order to determine the thermoelectric performance, we calculated the ZT for both the compounds as shown in Figs. 17(c) and 17(d). We observe that the ZT of the p-type LaAgSeO is higher than that of the n-type LaAgSeO. Contrastingly, in the case of LaAgTeO, n-type exhibits higher ZT than p type. More generally, LaAgTeO dominates with higher ZT over LaAgSeO for both types of doping. In LaAgSeO, the c direction is more favorable than the a direction for both types of doping. Also, for p-type LaAgTeO, the a direction is more favorable, whereas, for n-type LaAgTeO, the c direction is more favorable. The highest ZT for n-type LaAgTeO is 2.8 and the same is 1.24 for p-type LaAgSeO at $T = 900$ K which is higher than other oxide thermoelectric materials, such as Ca$_3$CO$_4$O$_9$ (0.87) at 973 K [59], Ca$_4$Sb$_2$O (1.32) at 1000 K [51], Na$_x$CoO$_{2-\delta}$ (1.2) at 800 K [48] and BiCuSeO (1.4) at 923 K [9]. Although a large power factor is observed with p-type doping, the high electronic thermal conductivity

FIG. 17. The calculated power factor (a) and (b) and thermoelectric figure of merit (c) and (d) of LaAgXO at $T = 900$ K for both p-type and n-type carriers.

suppresses the thermoelectric performance of holes for both compounds. In particular, the extraordinarily high ZT along the c direction of n-type LaAgTeO is caused by the low κ_e combined with ultralow κ_l. We reach the conclusion that, in terms of TE performance, n-type doping would be a better option for LaAgTeO. In LaAgSeO, however, both doping types would result in better performance with p-type doping showing a little advantage over n-type doping.

IV. CONCLUSION

In this paper, we have studied the transport properties of LaAgSeO and LaAgTeO within the framework of density functional theory and Boltzmann transport theory. The electronic structure and the transport properties are studied for both compounds. From the electronic structure perspective, LaAgTeO has a higher power factor compared to LaAgSeO. Both the investigated compounds show good thermoelectric performance at high temperatures. Furthermore, the intrinsic lattice thermal conductivity found to be ultralow in both LaAgXO compounds with $\kappa_l \approx 0.18$ W/mK along the c direction. We observed an interesting topological feature in phonon band dispersion and confirm the existence of a nodal ring on the Γ-X-M-Γ plane. It will be of interest to study the topological properties of the phonons in these compounds. We observed a high ZT value of 1.24 in p-type LaAgSeO and 2.8 in n-type LaAgTeO along the out-of-plane c direction at 900 K which highlights that these compounds exhibit excellent thermoelectric properties. We would like to note that along with lattice thermal conductivity, the electronic part of thermal conductivity also plays a crucial role in determining the TE characteristics. Although the higher scattering rates reduce the conductivity of electrons, it also limits the electronic thermal conductivity which favors the extraordinary TE performance in the case of n-type LaAgTeO. These findings indicate that scattering of carriers play an intriguing role in our compounds and warrant further careful experimental studies. We predict that with a proper choice of doping and other band engineering techniques, these compounds could be the suitable candidates for next generation thermoelectric material. Key challenges will be identifying suitable dopants and optimizing the carrier concentrations.
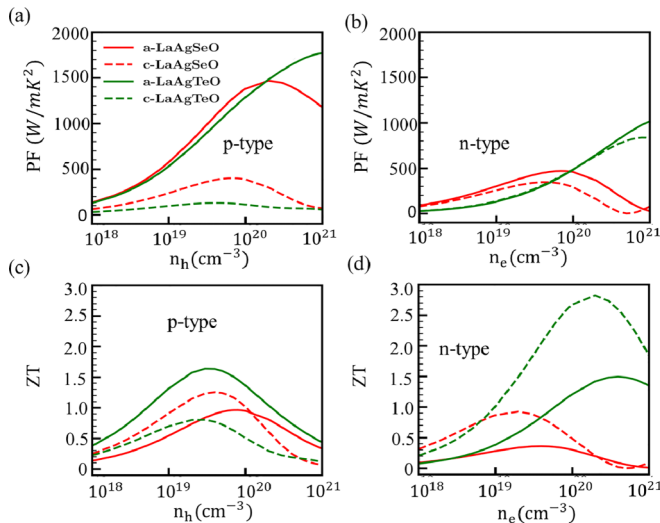
[1] G. A. Slack, Solid State Phys. **34**, 1 (1979).

[2] L. E. Bell, Science **321**, 1457 (2008).

[3] J. He and T. M. Tritt, Science **357**, 1369 (2017).

[4] E. Toberer, Nat. Energy **1**, 16172 (2016).

[5] L. Shen, X. Pu, Y. Sun, and J. Chen, Energy **113**, 9 (2016).

[6] X. Liu, Y. D. Deng, Z. Li, and C. Q. Su, Energy Convers. Manage. **90**, 121 (2015).

[7] M. Hyland, H. Hunter, J. Liu, E. Veety, and D. Vashaee, Appl. Energy **182**, 518 (2016).

[8] G. J. Snyder and E. S. Toberer, Nature Mater. **7**, 105 (2008).

[9] N. Wang, M. Li, H. Xiao, Z. Gao, Z. Liu, X. Zu, S. Li, and L. Qiao, npj Comput. Mater. **7**, 18 (2021).

[10] W. Khan, S. Azam, M. B. Kanoun, and S. Goumri-Said, Solid State Sci. **58**, 86 (2016).

[11] K. Ueda, H. Hiramatsu, H. Ohta, M. Hirano, T. Kamiya, and H. Hosono, Phys. Rev. B **69**, 155305 (2004).

[12] S. Tippireddy, D. S. P. Kumar, S. Das, and R. C. Mallik, ACS Appl. Energy Mater. **4**, 2022 (2021).

[13] N. Wang, M. Li, H. Xiao, X. Zu, and L. Qiao, Phys. Rev. Appl. **13**, 024038 (2020).

[14] M. Einhorn, B. A. D. Williamson, and D. O. Scanlon, J. Mater. Chem. A **8**, 7914 (2020).

[15] F. Q. Wang, Y. Guo, Q. Wang, Y. Kawazoe, and P. Jena, Chem. Mater. **29**, 9300 (2017).

[16] L. Zhu, G. Zhang, and B. Li, Phys. Rev. B **90**, 214302 (2014).

[17] R. Viennois, P. Hermet, M. Beaudhuin, J. L. Bantignies, D. Maurin, S. Pailhes, M. T. Fernandez-Diaz, M. M. Koza, C. Barreteau, N. Dragoe, and D. Berardan, J. Phys. Chem. C **123**, 16046 (2019).

[18] R. Guo, X. Wang, Y. Kuang, and B. Huang, Phys. Rev. B **92**, 115202 (2015).

[19] L. D. Hicks and M. S. Dresselhaus, Phys. Rev. B **47**, 16631 (1993).

[20] P. Graziosi, C. Kumarasinghe, and N. Neophytou, J. Appl. Phys. **126**, 155701 (2019).

[21] V. V. Bannikov, I. R. Shein, and A. L. Ivanovskii, Solid State Sci. **14**, 89 (2012).

[22] G. Kresse and J. Furthmüller, Phys. Rev. B **54**, 11169 (1996).

[23] G. Kresse and J. Furthmüller, Comput. Mater. Sci. **6**, 15 (1996).

[24] G. Kresse and J. Hafner, Phys. Rev. B **47**, 558(R) (1993).

[25] P. E. Blöchl, Phys. Rev. B **50**, 17953 (1994).

[26] J. P. Perdew, K. Burke, and M. Ernzerhof, Phys. Rev. Lett. **77**, 3865 (1996).

[27] H. J. Monkhorst and J. D. Pack, Phys. Rev. B **13**, 5188 (1976).

[28] S. Grimme, J. Antony, S. Ehrlich, and S. Krieg, J. Chem. Phys. **132**, 154104 (2010).

[29] S. Grimme, S. Ehrlich, and L. Goerigk, J. Comput. Chem. **32**, 1456 (2011).

[30] A. Togo and I. Tanaka, Scr. Mater. **108**, 1 (2015).

[31] K. Parlinski, Z. Q. Li, and Y. Kawazoe, Phys. Rev. Lett. **78**, 4063 (1997).

[32] A. Togo, F. Oba, and I. Tanaka, Phys. Rev. B **78**, 134106 (2008).

[33] A. M. Ganose, J. Park, A. Faghaninia, R. Woods-Robinson, K. A. Persson, and A. Jain, Nat. Commun. **12**, 2222 (2021).

[34] See Supplemental Material at http://link.aps.org/supplemental/10.1103/PhysRevMaterials.7.025405 for k-point convergence, q-mesh convergence, relative scattering for ADP, IMP, and POP and sound velocities from elastic constants and phonon dispersions for LaAgXO.

[35] S. Singh, L. Langa, V. Dovale-Fareloa, U. Heratha, P. Tavadzea, F. C. X. Coudertc, and A. H. Romeroa, Comput. Phys. Commun. **267**, 108068 (2021).

[36] A. Togo, L. Chaput, and I. Tanaka, Phys. Rev. B **91**, 094306 (2015).

[37] R. Pottgen and D. Johrendt, Z. Naturforsch. **63b**, 135 (2008).

[38] G. Liu, H. Sun, J. Zhou, Q. Li, and X. G. Wan, J. Appl. Phys. **119**, 185109 (2016).

[39] H. Hiramatsu, H. Yanagi, T. Kamiya, K. Ueda, and K. M. Hirano, H. Hosono, Chem. Mater. **20**, 326 (2008).

[40] M. Mukherjee and A. K. Singh, ACS Appl. Mater. Interfaces **12**, 8280 (2020).

[41] P. Vaqueiro, R. A. R. Al Orabi, S. D. N. Luu, G. Guélou, A. V. Powell, R. I. Smith, J.-P. Song, D. Weeb, and M. Fornari, Phys. Chem. Chem. Phys. **17**, 31735 (2015).

[42] Z. Feng, Y. Fu, Y. Zhang, and D. J. Singh, Phys. Rev. B **101**, 064301 (2020).

[43] J. R. Sootsman, D. Y. Chung, and M. G. Kanatzidis, Angew. Chem. Int. Ed. **48**, 8616 (2009).

[44] M. Born, Math. Proc. Cambridge Philos. Soc. **36**, 160 (1940).

[45] C. Li and Z. Wang, Adv. Sci. Tech. Mn + 1AXn Phases. 197 (2012).

[46] H. S. Ji, A. Togo, M. Kaviany, I. Tanaka, and J. H. Shim, Phys. Rev. B **94**, 115203 (2016).

[47] A. A. El-Sharkawy, A. M. A. Ei-Azm, M. I. Kenawy, A. S. Hillal, and H. M. Abu-Basha, Int. J. Thermophys. **4**, 261 (1983).

[48] K. Fujita, T. Mochida, and K. Nakamura, Jpn. J. Appl. Phys., Part 1 **40**, 4644 (2001).

[49] M. Ohtaki, K. Araki, and K. Yamamoto, J. Electron. Mater. **38**, 1234 (2009).

[50] S. Ohta, T. Nomura, H. Ohta, and K. Koumoto, J. Appl. Phys. **97**, 034106 (2005).

[51] W. Rahim, J. Skelton, and D. Scanlon, J. Mater. Chem. A **9**, 20417 (2021).

[52] J. Li, W. Zhai, C. Zhang, Y. Yan, P.-F. Liu, and G. Yang, Mater. Adv. **2**, 4876 (2021).

[53] D. D. Fan, H. J. Liu, L. Cheng, J. Zhang, P. H. Jiang, J. Wei, J. H. Liang, and J. Shi, Phys. Chem. Chem. Phys. **19**, 12913 (2017).

[54] G. H. K. Madsen, J. Carrete, and M. J. Verstraete, Comput. Phys. Commun. **231**, 140 (2018).

[55] W. Chen, J.-H. Pohls, G. Hautier, D. Broberg, S. Bajaj, U. Aydemir, Z. M. Gibbs, H. Zhu, M. Asta, G. J. Snyder, B. Meredig, M. A. White, K. Persson, and A. Jain, J. Mater. Chem. C **4**, 4414 (2016).

[56] I. R. Panneerselvam, M. H. Kim, C. Baldo, Y. Wang, and M. Sahasranaman, Phys. Chem. Chem. Phys. **23**, 23288 (2021).

[57] J. Cao, J. D. Querales-Flores, A. R. Murphy, S. Fahy, and I. Savic, Phys. Rev. B **98**, 205202 (2018).

[58] J. Ma, Y. Chen, and W. Li, Phys. Rev. B**97**, **97**, 205207 (2018).

[59] M. Shikano and R. Funahashi, Appl. Phys. Lett. **82**, 1851 (2003).